Improved Energy Resolution Measurements of Electron Precipitation Observed during an IPDP-type EMIC event

M. A. Clilverd[1], C. J. Rodger[2], A. T. Hendry[2,1], A. R. Lozinski[1,6], J-A. Sauvaud[3], M. R. Lessard[4], and T. Raita[5]

[1]British Antarctic Survey (UKRI-NERC), United Kingdom. [2]University of Otago, New Zealand. [3]Institut de Recherche en Astrophysique et Planétologie (IRAP), Toulouse, France. [4]University of New Hampshire, USA. [5]Sodankylä Geophysical Observatory, University of Oulu, Finland. [6]Now at University of California, Los Angeles, USA

Corresponding author: Mark Clilverd (macl@bas.ac.uk)

Key Points:

- An electromagnetic ion cyclotron wave event (an interval of pulsations with diminishing period, IPDP) was studied from Low Earth Orbit
- Co-incident satellite observations detected IPDP-induced energetic electron precipitation, starting at 150 keV, peaking at 215 keV
- High-resolution measurements from the DEMETER satellite show enhanced fluxes from 215 keV to 1.5 MeV exhibiting a 'hard' power-law spectrum

Abstract

High energy resolution DEMETER satellite observations from the Instrument for the Detection of Particle (IDP) are analysed during an electromagnetic ion cyclotron (EMIC)-induced electron precipitation event. Analysis of an Interval Pulsation with Diminishing Periods (IPDP)-type EMIC wave event, using combined satellite observations to correct for incident proton contamination, detected an energy precipitation spectrum ranging from ~150 keV to ~1.5 MeV. While inconsistent with many theoretical predictions of >1 MeV EMIC-induced electron precipitation, the finding is consistent with an increasing number of experimentally observed events detected using lower resolution integral channel measurements on the POES, FIREBIRD, and ELFIN satellites. Revised and improved DEMETER differential energy fluxes, after correction for incident proton contamination shows that they agree to within 40% in peak flux magnitude, and 85 keV (within 40%) for the energy at which the peak occurred as calculated from POES integral channel electron precipitation measurements. This work shows that a subset of EMIC waves found close to the plasmapause, i.e., IPDP-type rising tone events, can produce electron precipitation with peak energies substantially below 1 MeV. The rising tone features of IPDP EMIC waves, along with the association with the high cold plasma density regime, and the rapidly varying electron density gradients of the plasmapause may be an important factor in the generation of such low energy precipitation, co-incident with a high energy tail. Our work highlights the importance of undertaking proton contamination correction when using the high-resolution DEMETER particle measurements to investigate EMIC-driven electron precipitation.

Plain Language Summary

Energetic electrons are lost rapidly from the outer radiation belt. Several processes are thought to drive the electron losses. One process is through interactions with electromagnetic ion cyclotron (EMIC) waves. Theoretical studies suggest that electrons primarily with energy >1 MeV are lost through this process, however, previous experimental satellite observations indicate that precipitation bursts with much lower electron energies are more common. One issue is that the previous satellite observations were made with poor energy resolution and are challenging to interpret due to coincident proton precipitation, which contaminate the electron measurements. Here we use observations from the DEMETER satellite which we have corrected for proton contamination. The measurements, made with higher energy resolution than before, confirm that indeed, low energy electron precipitation can happen when EMIC waves drive electron losses. The study finds that this lower energy characteristic is likely to be driven by a small subset of rising tone EMIC waves, known as Interval Pulsation with Diminishing Periods (IPDP), typically confined to the magnetic local time evening sector.

1 Introduction

The dynamical behavior of energetic electron fluxes in the outer radiation belt involves the loss of electrons into the atmosphere – a process known as electron precipitation. Quantifying and characterizing energetic electron precipitation (EEP, i.e., >10 keV) is one of the requirements for a more complete description of solar forcing that can be used in coupled climate models (Seppälä et al., 2015; van de Kamp et al., 2016; Matthes et al., 2017; Duderstadt et al., 2021; Nesse Tyssøy et al., 2021; Salice et al., 2024). Electrons precipitating with energies >10 keV will typically deposit their energy in the atmosphere at altitudes of 100 km or below (Turunen et al., 2009; Xu et al., 2020; Katoh et al., 2023), leading to chemical and dynamical changes in the climate system (Brasseur and Solomon, 2005; Andersson et al., 2012; Sinnhuber et al., 2012; Mironova et al., 2015; Orsolini et al., 2018; Guttu et al., 2021). One mechanism that causes energetic electron precipitation is via scattering with EMIC waves (e.g., Thorne and Kennel, 1971; Millan & Thorne, 2007; Denton et al., 2019). Many theoretical predictions of EMIC-induced electron precipitation suggest that fluxes primarily occur with energy > 1 MeV (e.g., Thorne and Kennel, 1971; Summers & Thorne, 2003). However, recent observational studies contradict the theoretical predictions (Hendry et al., 2017; Hendry et al., 2021a; Capannolo et al., 2021; Capannolo et al., 2023) through the identification of EMIC-induced electron precipitation with energies starting from 100's of keV. This area of study has been investigated extensively by Denton et al. (2019) through numerical simulations, although no definitive mechanism for the generation of peak energies <1 MeV has been identified to date. Hanzelka et al. (2023, 2024) used test particle simulations of fractional sub-cyclotron resonant interactions with EMIC waves to generate sub-MeV electron precipitation consistent with some of the ELFIN cubesat observations described in Capannolo et al. (2023). The presence of lower energy precipitation is particularly important when considering the impact of observed EMIC-induced losses on radiation belt populations (e.g., Us**a**nova et al., 2014; Hendry et al., 2021a) and resultant atmospheric ozone decreases (Hendry et al., 2021b).

EMIC waves have been observed using instruments flown on spacecraft as well as by instruments located on the ground. The waves occur over a wide range of geomagnetic latitudes, a wide range of magnetic local time (MLT), and exhibit a range of temporal behavior (e.g., see Figure 6 in Fukunishi et al., 1981). Spacecraft-based observations of EMIC waves can be limited by the transitory nature of the measurements, particularly in the case of temporal changes in wave amplitude or frequency (e.g., Rodger et al., 2015). Such EMIC waves are often observed in the 0.1-2 Hz range with ground-based induction coil magnetometers. Several distinct wave types have been classified, including periodic emissions, emission bursts, ion-cyclotron chorus, and IPDP waves (Fukunishi et al., 1981). Whether the temporal structure within each wave-type produces different characteristics in the resultant EEP remains an open question. Kubota & Omura (2017) investigated the effects of rising tone EMIC emissions on electron populations near the plasmapause using test particle simulations. The calculations showed that while rising tone EMIC wave subpackets could produce significant fluxes of precipitating particles with energy <1 MeV, the process required extremely large wave amplitudes (> 10 nT) and thus offered an unlikely explanation for the satellite observations.

The *L*-shell and magnetic local time distribution of EMIC waves has been studied extensively through spacecraft observations (Min et al., 2012; Meredith et al., 2014; Saikin et al., 2015; Wang et al., 2017; Jun et al., 2021; Allen et al., 2015; Grison et al., 2021). Meredith et al. (2014) combined observations from the CRRES satellite to form detailed MLT "clock plots" of wave power. That wave database has been recently extended to include more satellite observations and produce updated MLT clock plots (Ross et al., 2021). Strong EMIC waves are mostly found on the dayside of the magnetosphere, typically around MLT noon as well as in the early afternoon, and at *L*-shells substantially higher than the plasmapause, i.e., *L*=5 – 6. EMIC waves in these latitudes, and MLT ranges, would likely be classified as periodic, burst, or ion-cyclotron chorus emissions (Fukunishi et al., 1981). Strong EMIC waves, but with low occurrence rates, were also identified at lower *L*-shells, close to the average position of the plasmapause, i.e., *L*=4, in the MLT evening sector, about 22 MLT. These would be likely to be classified as IPDP waves. The generation of IPDP-type EMIC waves is known to be associated with substorm injection of 50 - 100 keV protons close to MLT midnight (Salzano et al., 2022 and references therein). The protons subsequently drift in longitude westwards from the injection region (i.e., drift anti-clockwise in MLT) accompanied by inward motion driven by electric field convection (Gendrin et al., 1967; Fukunishi, 1969). Large Pc 1-2 wave growth through cyclotron resonance occurs when the drifting protons intersect the cold plasma density gradients associated with the plasmapause or plasmaspheric plumes. This ‘cartoon’ picture explains three of the main characteristics of IPDP waves, namely, that they typically occur in the evening MLT sector, close to the location of the plasmapause (or possibly plasmaspheric plumes), and are delayed with respect to the onset timing of substorms. Another key characteristic of IPDP's is the gradual increase of observed wave frequency over time. Rates of change are usually observed to be 0.3 - 2 Hz/hour (Fraser and Wawrzyniak, 1978; Salzano et al., 2022).

Ground-based measurements of very low frequency (VLF) radio waves, propagating sub-ionospherically from distant transmitters, showed the potential of EMIC waves to generate excess ionization below the D-region of the ionosphere (Rodger et al., 2008). Analysis of sub-ionospheric radio signals by Clilverd et al. (2010) showed a link between temporal variations of electron precipitation and the POES satellites bounce-loss-cone fluxes. To investigate EMIC wave-induced EEP in the POES satellite measurements, a large database of events was created using a detection algorithm based on simultaneous proton and electron precipitation characteristics (Sandanger et al., 2009; Carson et al., 2013). The proton channel used was the P1 52 keV differential flux channel, and the electron channel used was the P6 detector - which suffers from >700 keV electron contamination (Evans and Greer, 2004; Yando et al., 2011). In this study we hereafter refer to the P6 0˚ telescope flux as the E4 detector, using the nomenclature suggested by Peck et al., 2015, representing >~700 keV precipitating electrons. Most of the events occurred in the MLT evening sector or close to midnight. Few were identified around MLT noon. This is consistent with an association with IPDPs, and also consistent with the earlier work of Miyoshi et al. (2008). Hendry et al. (2016) reported that a significant proportion, as high as 90% of the POES events exhibiting simultaneous proton and electron precipitation correspond with EMIC wave detections on the ground. That study also indicated that the EMIC waves linked to these precipitation events tended to be IPDP.

The current state of research into EMIC-induced electron precipitation poses two questions: what does the spectrum of EMIC-induced electron precipitation events look like; and what are the characteristics of the EMIC waves that drive low energy (≲250 keV) electron precipitation? To address these questions, we make use of DEMETER satellite IDP observations. DEMETER only observed locally precipitating electron fluxes when orbiting in the region of the North Atlantic Ocean, where the bounce-loss-cone is larger than the viewing angle subtended by the telescope (see Figure 2 in Whittaker et al., 2013). We analyze the EEP for an IPDP EMIC event which occurred late on 11 April 2005 and was clearly observed with ground-based induction coil magnetometers. During the IPDP event DEMETER's orbit passed through the precipitation region just after 21 UT, i.e., at 22 MLT. Using co-located POES NOAA-17 satellite measurements of proton fluxes provides the means to remove the impact of proton contamination from the DEMETER IDP measurements. As with the integral channel analysis of NOAA-17, a wide energy range of electron precipitation was observed with a peak in flux between 200 – 300 keV.

2 Observations

DEMETER IDP operated from 2004 – 2010 and measured 126 differential energy channels from 50 keV to 2 MeV (Sauvaud et al., 2013) in 17.8 keV steps. Here we use 124 of the energy channels, following previous authors by dropping the first and the last channels (Whittaker et al, 2013). To avoid electromagnetic disturbances caused by the Solar Array Drive Mechanism (SADM) on the DEMETER scientific instruments, the SADM was only switched ON over the polar regions to orient its Solar Array Generator toward the Sun. SADM operation was limited to periods when the satellite was at latitudes >65° and <−65°. As a result, scientific instrument data were not collected in the polar regions (Cussac et al., 2006).

To investigate the DEMETER satellite IDP measurements for locally precipitating electron fluxes, the analysis was restricted to times when the satellite was observing above a region of the North Atlantic (Whittaker et al., 2013), when ground-based induction coil magnetometer observations confirmed the presence of EMIC waves. To the east of the North Atlantic region we make use of the Nurmijärvi pulsation magnetometer in Finland, located at L~3.4 (Yahnin et al., 2017). The magnetometer is operated by the Sodankylä Geophysical Observatory. To the west of the North Atlantic region we consider the magnetic field-line conjugate location of the southern hemisphere pulsation magnetometer at Halley, Antarctica

(Engebretson et al., 2008), which is located at *L*~4.5. Our wave analysis concentrates on the frequency range of 0.1–2 Hz, in which Pc1-2 waves, including IPDP waves, are known to occur. The induction coil magnetometers sample at a rate of 40 sample/s, and use is made of spectrograms showing wave activity in the Pc 1-2 range to identify occurrences of IPDP.

3 Methods

In the DEMETER IDP instrument a 6 μm aluminum foil protects the semi-conductor from UV and from low-energy protons (Sauvaud et al., 2013). As a result of the foil, the detector is sensitive to contaminating protons with >500 keV energies. Typically the proton flux in that energy range is considerably lower than that of low-energy electrons, particularly when DEMETER views the more populated drift-loss-cone. However, in this particular study the limitation of viewing only the bounce-loss-cone in the North Atlantic results in electron flux levels that are often close to the sensitivity limit of the instrument, during events where strong proton precipitation is expected. Thus, proton contamination is potentially more of an issue than originally envisaged.

Fortunately, DEMETER flew in a similar orbit configuration to the POES satellites, i.e., nearly circular at ~650-850 km altitude, polar orbiting, Sun-synchronous. As EMIC waves are strongly associated with low energy proton precipitation (e.g., Sandanger et al., 2009; Ni et al., 2023), and there were no independent proton measurements made on DEMETER to assess the proton flux levels, we follow the suggestion of Sauvaud et al. (2013) in using measurements of proton fluxes observed by POES SEM-2 particle instruments when DEMETER and a POES spacecraft are in close-conjunction. We use the multi-layered shielding simulation software

(MULASSIS) transport code (Lei et al., 2002; Lozinski et al., 2019) to simulate the attenuation effect of 6 µm aluminum foil on a proton spectrum determined from near coincident and conjunct POES measurements. The attenuated particle fluxes are treated as contamination and removed from those measured by DEMETER IDP, leaving a revised and improved measure of precipitating electron flux.

4 Case study of EMIC-induced electron precipitation

Based on the selection criteria described in section 2, a DEMETER – POES conjunction was found that met all the specified requirements. This event occurred on 11 April 2005 at 21:14 UT. Figure 1 shows a map of the North Atlantic region. The DEMETER (blue trace) and NOAA 17 (red trace) orbital paths, and the locations of the satellites during the near-conjunction are shown (circles). Induction coil magnetometer observatory locations are shown, representing Nurmijärvi in Finland to the east of the study region, and the conjugate point of Halley, Antarctica, to the west of the region. An L=4 contour is shown by the dashed black line. The blue DEMETER trace ends just north of the event location close to L=4 because DEMETER observations were usually not made at high latitudes (i.e., the satellite instrumentation was switched off).

Figure 2 presents the observations during the 11 April 2005 event. NOAA-17 flux variations along the orbital path from 21:13:00 UT to 21:16:00 UT are shown. The blue trace represents the E4 >700 keV flux. The red trace represents the P1 0˚ telescope flux (30-80 keV precipitating protons). Some POES-contaminating high energy protons, i.e., as detected by the P6 telescope, were observed during this event, but were successfully removed (following techniques described earlier in Hendry et al., 2016). Elevated E4 flux at 21:14:15 UT coincides with a smaller peak in P1 flux. This is characteristic of EMIC-induced electron precipitation (Sandanger et al., 2009; Hendry et al., 2016). The enhancement in E4 flux is only observed for ~6 s. At POES NOAA-17 altitudes and *L*~4 this duration is equivalent to a precipitation feature with a latitudinal width of ~0.1 *L*. Figure 2 also shows that later, after 21:14:30 UT, a broader elevated P1 flux feature with low E4 flux levels occurs at L~5-6. This feature is more consistent with potential ring current precipitation.

Figure 3 shows the DEMETER IDP electron flux at 21:13:34 UT, measured just prior to the instrument being turned off as DEMETER approached higher latitudes. Non-zero flux is observed from the lowest energy channel (80 keV) up to 1500 keV, with the peak flux occurring around 200 keV. At energies above the peak flux, a gradual decrease in flux is observed, declining towards zero. At energies below the peak flux a sharp decrease in flux occurs compared to the peak levels, but non-zero flux is never achieved. At the time of the event DEMETER was approaching *L*=4 while NOAA-17 encountered its EMIC-induced precipitation signature at *L*=4 some 40 s later. Because of the potential for the IDP detector to be contaminated by protons the key question posed here is what component of the DEMETER IDP fluxes in Figure 3 were caused by electrons and what was due to proton contamination?

Figure 4 presents two panels depicting the ground-based observations of EMIC wave activity during the electron precipitation event on 11 April 2005. The upper panel shows the H-component (horizontal intensity) induction coil measurement from Nurmijarvi in Finland (*L*=3.4) situated to the east of the satellites during the event. IPDP-type EMIC waves, i.e., gradually increasing frequency of wave features, were observed Nurmijarvi. Similar wave features were observed in the D- and Z-component spectral plots. The majority of the wave power at ~1 Hz had a left-handed polarization at the time of the event (not shown), typical for EMIC waves

(Usanova, 2021 and references therein). The wave event onset at frequencies of ~0.1-0.2 Hz at about 18:30 UT, rising gradually to nearly 2 Hz at about 22:00 UT. A white dashed line indicates a rising frequency feature, with a rate of ~0.6 Hz/hour, consistent with typical IPDP rates (Fraser and Wawrzyniak, 1978; Salzano et al., 2022). A vertical white arrow indicates the time of the electron precipitation event seen by DEMETER and POES N17. At that time enhanced wave power can be seen from 0.5 Hz to 1.5 Hz.

The lower panel of Figure 4 shows simultaneous H-component induction coil measurements from Halley in Antarctica (L=4.5), whose magnetic field line conjugate lies to the west of the satellite locations at the time of the event – as shown in Figure 1. As in the upper panel a white dashed line indicates a rising frequency feature of ~0.6 Hz/hour but in this case it is delayed with respect to Nurmijarvi by about 1 hour. The precipitation event time identified by the white vertical arrow indicates EMIC wave power from 0.1 Hz to 0.5 Hz at Halley, with weaker amplitude waves observable up to ~1 Hz around the time of the event. Some individual rising tone features can be seen within the general envelope wave power, with slightly faster rates of ~1 Hz/hour.

The result of removing the proton contamination of the IDP measurements is presented in Figure 5. The red line shows the NOAA-17 proton flux spectra as described by a double Maxwellian energy distribution fitted to the NOAA-17 proton channels following the approach of Peck et al. (2015). The contamination of the DEMETER IDP instrument due to those proton fluxes, after accounting for the protection afforded by the 6 μm aluminum foil using the MULASSIS code, is shown by the green dashed line. The solid blue line shows the IDP measurement at the time of the IPDP-induced precipitation. Two features can be noted, namely that the IDP flux and the contamination flux levels are similar at energies below ~150 keV, while IDP electron fluxes are significantly higher than the contamination fluxes above ~150 keV.

Figure 6 shows the corrected IDP electron precipitation flux (blue line) with 20% uncertainty ranges, following Sauvaud et al. (2013), indicated by blue dotted lines. At energies below ~150 keV the IDP fluxes are close to zero, while the peak flux occurs at ~215 keV at levels of ~100 el. $s^{-1}cm^{-2}sr^{-1}keV^{-1}$. Enhanced electron precipitation fluxes occur at energies up to ~1.5 MeV. Also shown on the panel are the electron precipitation flux calculated from the integral channels of NOAA-17 (black line) following the fitting technique of Hendry et al. (2017). Hendry et al. fitted the four POES integral electron flux measurements with a distribution peaked around a central energy whilst taking into account the energy-dependent geometric factors determined by Yando et al. (2011), and compensating for any proton contamination. The peaked flux distribution (J) was calculated as a function of energy (E) using the relationship:

$$J = (\exp(\alpha_1 - \beta_1 \log(E)) + \exp(-\alpha_2 + \beta_2 \log(E)))^{-1}$$

Where in this case α_1=34.2, β_1=7.1, α_2=16.7, β_2=2.0, determined using a least squares fit to the integral measurements and restricted to one decimal place as in Hendry et al. (2017). The values α_1 and β_1 describe the characteristics of the spectral rise to the peak flux, while α_2 and β_2 describe the spectral characteristics for energies higher than that of the peak flux.

An uncertainty of 20% in the NOAA-17 electron flux spectrum is indicated by dashed black lines, based on the least squares error in fitting the above distribution to each of the integral channels. The peak energy of the NOAA-17 flux distribution occurs at 300 keV, with a peak flux of ~140 el. $s^{-1}cm^{-2}sr^{-1}keV^{-1}$. Above ~400 keV the DEMETER IDP electron fluxes are approximately a factor of two lower than those calculated using the integral NOAA-17 detectors using the technique of Hendry et al. (2017). The high-resolution differential DEMETER IDP measurements indicate that while the POES integral electron channel data can be used to determine the general characteristics of the IPDP-induced electron precipitation, some refinement in the integral channel analysis would be beneficial. This will likely be important when estimating the impact of EMIC-driven electron precipitation on polar atmospheric chemistry and trapped radiation belt fluxes, for example as earlier undertaken by Hendry et al. (2021b).

Despite the lack of exact agreement in the event flux characteristics between DEMETER and the more approximate POES integral channel analysis, it is illuminating to investigate if the corrected DEMETER IDP flux variation can be described by a peak exponential distribution, as assumed for the POES analysis. Figure 7 shows how successfully a peak exponential distribution fits the corrected IDP fluxes. The upper panel shows the corrected IDP (blue line) and the modelled peak exponential distribution (black line) where α_1=73.27, β_1=14.90, α_2=14.15, β_2=1.77. Good agreement is seen apart from at energies close to 100 keV. This discrepancy is probably due to a slight underestimate of the contaminating proton flux as is apparent in Figure 5.

The lower panel of Figure 7 shows a power law fit (red line) to the corrected IDP fluxes above the energy of the peak flux (215 keV). The fit shows a high value of correlation (Pearson correlation coefficient R^2 = 0.977 for 78 data points) up to 1.59 MeV. Above 1.59 MeV the IDP data shows increasing scatter, suggesting some influence from the instrument noise floor.

5 Discussion

Detailed analysis of DEMETER satellite measurements during an electron precipitation event driven by an IPDP-type EMIC wave on 11 April 2005 shows that the largest flux occurred at an energy of 215 keV. While inconsistent with many theoretical predictions of EMIC-induced electron precipitation occurring primarily with energy > 1 MeV (Thorne and Kennel, 1971; Summers & Thorne, 2003), the finding here is consistent with an increasing number of experimental studies; the large number of events described in Carson et al. (2013) based on POES integral channel measurements, Hendry et al. (2017) using POES and DEMETER, Capannolo et al. (2021) using FIREBIRD II, and Capannolo et al. (2023) using the ELFIN cubesats. The event studied here is typical of the EMIC-induced electron precipitation characteristics found by Carson et al. (2013), and Hendry et al. (2016), in that it occurs pre-midnight in MLT, close to the typical location of the plasmapause (L~4), and is associated with an IPDP-type rising frequency EMIC wave.

Hendry et al. (2017) analysed NOAA POES SEM-2 telescope measurements to determine the peak energy of the EEP involved. A maximum error algorithm was developed using detailed geometrical factors for each integral flux detector (E1 >30 keV, E2 >100 keV, E3 >300 keV and E4 >700 keV electrons). The peak energy of EMIC-induced EEP events were determined by assuming a peaked energy spectrum specified by two spectral indices, each one defining the slope either side of the peak flux. Hendry et al. (2017) found that >80% of the EMIC-induced precipitation events studied had a peak energy between 200 and 500 keV, while <20% had a peak energy >800 keV, although the energy resolution of the electron precipitation was poorly resolved because of the integral flux measurements. To investigate this issue a case study was undertaken with high energy resolution DEMETER satellite particle measurements made in conjunction with POES. An estimate of the background flux contamination of the

DEMETER measurements was made from observations prior to, and after, the precipitation event. The background flux was at least partly due to quasi-trapped electrons in the drift-loss-cone, and these needed to be removed to determine the locally precipitating fluxes. A peaked electron flux distribution was determined from the high resolution DEMETER data, with a flux maximum at 250 keV, declining with a power-law spectrum at energies above this. In-situ DEMETER wave data confirmed the presence of an EMIC wave at the time of the event.

Further, using thousands of events identified by the Carson et al. (2013) algorithm Hendry et al. (2021a) undertook a superposed epoch analysis of trapped radiation belt flux variations based on simultaneous Global Positioning System (GPS) particle measurements made over a wide range of energies. EMIC-induced EEP at the heart of the outer radiation belt ($4<L^*<5$) was observed to deplete trapped electron populations at 120 keV, 600 keV, and 1 - 6 MeV, consistent with the idea that many of the events involved <1 MeV precipitation fluxes.

In more recent studies, Capannolo et al. (2021) analysed FIREBIRD II measurements of energetic electron precipitation events associated with EMIC waves, and similarly identified EEP occurring in the 200 – 300 keV range, as well as at MeV precipitation. A multi-event analysis showed that the events occurred around the MLT dusk sector, with about 90% having EEP at energies <700 keV. However, in about half of the events the occurrence of co-incident proton contamination precluded any detailed electron spectrum analysis < 700 keV. This work was extended by Capannolo et al. (2023) using the ELFIN cubesat pair. Proton precipitation was used as a proxy for the presence of EMIC waves, and 144 electron precipitation events identified. Electron precipitation with energies of $\lesssim$250 keV was observed, coincident with ~MeV precipitation. Comparison with quasi-trapped flux levels showed that the lower energy precipitation could be described as occurring with weak scattering efficiency, while the higher energy electron precipitation occurred in events that exhibited strong scattering efficiency. This is consistent with the findings of Hendry et al. (2021a) based on GPS satellite dosimeter measurements of trapped electron fluxes in the presence of EMIC waves. Capannolo et al. (2023) were able to model the energy characteristics of the >250 keV electron precipitation using quasilinear theory incorporating the statistical characteristics of EMIC waves at $L\sim6$. However, the difficulty in reproducing the observed $\lesssim$250 keV electron precipitation contribution using quasilinear theory was put down to possible non-resonant interactions, other waves, or EMIC wave properties not described by the statistical wave characteristics. An et al. (2022, 2024) used a theoretical model of nonresonant scattering with short EMIC wave packets to show that it was possible to extend the energy of significant scattering well below the minimum resonance energy. Multiple in-situ wave observations, and careful one-to-one satellite conjunction analyses, has been called for to address this area of scattering well below the minimum resonance energy.

The two panels of Figure 4 confirm the presence of IPDP-type waves at the time of the precipitation, potentially driven by substorm injected protons from an event at 17:56 UT which had an onset location to the east of the North Atlantic region as determined by SuperMAG (Gjerloev, 2012; Ohtani and Gjerloev 2020). Figure 2 indicates that proton precipitation was occurring during the event, which would also be consistent with EMIC wave-induced precipitation (Sandanger et al., 2009). The delayed Halley IPDP wave feature is consistent with a westwards drifting proton interaction region (Clilverd et al., 2015), although some of the delay may have come from east-west ionospheric ducting acting over 10’s of degrees of longitude (Kim et al., 2010). It is noted here that coincident very low frequency (VLF) observations made at Halley (not shown) do not indicate any significant VLF wave power in the VLF whistler mode chorus and hiss bands, and thus whistler mode VLF waves are unlikely to contribute to any of the observed lower energy electron precipitation observed by DEMETER, as shown in Figure 3. This is consistent with the earlier report by Rodger et al. (2015), who combined POES, Van Allen Probes, and ground based measurements to investigate multiple EMIC-driven precipitation events. Rodger et al. found that the events exhibited peak precipitating electron fluxes at energies a few hundred keV. High-quality wave observations made near the geomagnetic equator by the Van Allen Probes found no evidence of whistler mode waves causing the scattering, only the EMIC waves seen at the spacecraft. Shen et al. (2023) undertook a simulation of loss cone filling by whistler-mode chorus emissions that resulted in loss cone filling at energies from 5 keV to 500 keV even with very weak waves (< 20 pT). Therefore, it may be possible that the unexplained IDP fluxes at <150 keV shown in Figure 6 could have been caused by the presence of undetected, weak whistler waves.

In the lower panel of Figure 7 the EMIC-induced precipitation power law slope is given by a spectral gradient of k= -1.77. In previous studies Clilverd et al. (2020) used a spectral gradient of k= -3 to -4 (average k= -3.5) to represent the electron precipitation flux during a geomagnetic storm, which was assumed to be dominated by whistler-mode chorus-driven precipitation. As such the electron precipitation from this EMIC IPDP event is 'hard' because it contains relatively large fluxes at high energy compared to lower energies. Analysis of a large POES electron flux dataset undertaken by van de Kamp et al. (2016) also showed spectral gradients of k= -3 to -4 during enhanced electron precipitation, outside of the plasmapause. Analysing the POES electron flux dataset as a function of magnetic local time (MLT) van de Kamp et al. (2018) confirmed the spectral gradient findings of k= -3 to -4 where VLF whistler-mode chorus driven electron precipitation was expected to occur (morning MLT – see Figure 3 of that paper). However, for evening sector times (18-24 MLT), spectral gradients close to the location of the plasmapause were close to *k*= -2. This is consistent with the findings in this study and Hendry et al. (2017), where evening MLT sector, plasmapause EMIC IPDP electron precipitation events generate a ‘hard’ electron precipitation spectrum – unlike that expected for whistler-mode VLF chorus.

The identification of a band of electron precipitation in Figure 2 of ~0.1 *L* wide is slightly smaller than the electron precipitation radial scales of 0.3 *L* determined by Hendry et al. (2016) and Capannolo et al. (2023). However, the radial width is consistent with the recent work of Blum et al. (2024) where radially narrow (~0.1 *L*) EMIC wave regions were detected simultaneously with energetic electron precipitation using the Van Allen Probes and the CALorimetric Electron Telescope experiment onboard the International Space Station. Hendry et al. (2020) combined wave observations from the RBSP and ARASE satellites to determine the size of an EMIC wave source region, at *L*~4, and located close to the example here, i.e., over head of the UK, at about 21 UT. A wave source radial size of 0.7 *L* was determined. This suggests that in cases like the one studied here, the wave source region may be similar to, or slightly wider than, the electron precipitation region.

6 Conclusions

Detailed analysis of an IPDP-type EMIC wave event on 11 April 2005 using combined satellite and ground-based observations has shown that electron precipitation occurs with fluxes ranging from ~150 keV to ~1.5 MeV. Capannolo et al. (2023) suggested that in order to more accurately model the characteristics of electron precipitation at energies below 250 keV, EMIC wave properties not described by statistical wave characteristics could be required. This study provides a description of such wave characteristics, where the IPDP nature of the wave is associated with rising tone emissions. At the time of an electron precipitation event observed EMIC waves showed a rising tone feature of 0.6 Hz/hour, ranging from 0.1 Hz to 1.5 Hz. Some finer structure exhibited rate rises approximately double the overall envelope. On the ground, the wave was observed for ~3 hours.

Comparison between the high-resolution DEMETER IDP differential channel measurements of the IPDP-induced precipitation and the low-resolution integral channel measurements of POES satellites, shows that they agree to within 40% in their determination of peak flux magnitude, and 80 keV (<40%) in the energy at which the peak occurred. Our work highlights the importance of undertaking proton contamination correction when using the high-resolution DEMETER loss measurements to investigate EMIC-driven electron precipitation. In the case studied here, the peak energy of the electron precipitation occurred at slightly lower energy than found using the integral POES channels.

This study suggests that the POES integral channel energy spectrum fitting technique employed by Hendry et al. is reasonable and confirms the previous finding that many EMIC-induced electron precipitation events show peak energies <1 MeV (Hendry et al., 2017; 2021a). The lower energy (<1 MeV) electron precipitation association with IPDP wave events, and strong occurrence bias towards the MLT dusk sector, is consistent with the idea of injected protons drifting westwards from their near-midnight injection region, driving the required wave-particle resonance. It is also consistent with a role of high cold plasma density conditions within or at the outer edge of the plasmapause, which acts to reduce the resonant energy of the interactions (Hirai et al., 2023 and references therein). The spectral gradient of the precipitated electrons driven by the EMIC IPDP waves was found to be well described by a power law, with gradient k= -1.77. This is substantially harder than the spectral gradients associated with electron precipitation from VLF whistler-mode chorus regions, which is consistent with the absence of any observed chorus at the time of the EMIC event examined here.

Acknowledgments

The authors wish to thank the personnel who developed, maintain, and operate the NOAA/POES spacecraft and the earlier DEMETER satellite. Support for the Halley search coil magnetometer was provided by U.S. National Science Foundation grants PLR-1341493 to Augsburg College, and PLR-1341677 to the University of New Hampshire. Support at the University of New Hampshire was also provided by NSF grant 2133897. We gratefully acknowledge the SuperMAG collaborators (https://supermag.jhuapl.edu/info/?page=acknowledgement).

Open Research

The data used in this paper are available at NOAA's National Geophysical Data Center (NGDC - POES MEPED data, https://ngdc.noaa.gov/stp/satellite/poes/), and the CNES/CESR Centre de Donnees pour la Physique des Plasmas (CDPP - Demeter IDP, https://cdpp-archive.cnes.fr/user/cdpp/modules/1723). The Halley induction coil magnetometer data for this paper are available at the British Antarctic Survey Polar Data Centre (http://psddb.nerc-bas.ac.uk/data/access/). The Nurmijärvi induction coil magnetometer is part of the Finnish pulsation magnetometer network. Nurmijärvi magnetometer spectrograms are available at the Sodankylä Geophysical Observatory website (https://www.sgo.fi/Data/Pulsation/pulData.php).

References

Allen, R. C., J.-C. Zhang, L. M. Kistler, H. E. Spence, R.-L. Lin, B. Klecker, M. W. Dunlop, M. André, and V. K. Jordanova (2015), A statistical study of EMIC waves observed by Cluster: 1. Wave properties, J. Geophys. Res. Space Physics, 120, 5574–5592, doi:10.1002/2015JA021333.

An, X., Artemyev A., Angelopoulos, V., Zhang, X., Mourenas, D., & Bortnik, J. (2022). Nonresonant Scattering of Relativistic Electrons by Electromagnetic Ion Cyclotron Waves in Earth's Radiation Belts. American Physical Society, 129 (13), 135101-08, https://link.aps.org/doi/10.1103/PhysRevLett.129.135101

An, X., Artemyev, A., Angelopoulos, V., Zhang, X.-J., Mourenas, D., Bortnik, J., & Shi, X. (2024). Nonresonant scattering of energetic electrons by electromagnetic ion cyclotron waves: Spacecraft observations and theoretical framework. Journal of Geophysical Research: Space Physics, 129, e2023JA031863. https://doi.org/10.1029/2023JA031863

Andersson, M., Verronen, P. T., Wang, S., Rodger, C. J., Clilverd, M. A., & Carson, B. R., (2012). Precipitating radiation belt electrons and the production of mesospheric hydroxyl during 2004-2009. *J. Geophys. Res*., 117(D9), D09304, doi:10.1029/2011JD017246

Blum, L. W., Bruno, A., Capannolo, L., Ma, Q., Kataoka, R., Torii, S., & Baishev, D. (2024). On the spatial and temporal evolution of EMIC wave-driven relativistic electron precipitation: Magnetically conjugate observations from the Van Allen Probes and CALET. Geophysical Research Letters, 51,e2023GL107087. https://doi.org/10.1029/2023GL107087

Brasseur, G., & Solomon, S., (2005). *Aeronomy of the Middle Atmosphere*, 3rd ed., D. Reidel Dordrecht, Netherlands.

Capannolo, L., Li, W., Spence, H., Johnson, A. T., Shumko, M., Sample, J., & Klumpar, D., (2021). Energetic electron precipitation observed by FIREBIRD-II potentially driven by EMIC waves: Location, extent, and energy range from a multievent analysis. *Geophysical Research Letters*, 48, e2020GL091564. https://doi.org/10.1029/2020GL091564

Capannolo, L., Li, W., Ma, Q., Qin, M., Shen, X.-C., Angelopoulos, V., et al. (2023). Electron precipitation observed by ELFIN using proton precipitation as a proxy for electromagnetic ion cyclotron (EMIC) waves. *Geophysical Research Letters*, 50, e2023GL103519. https://doi.org/10.1029/2023GL103519

Carson, B. R., Rodger, C. J., & Clilverd, M. A., (2013). POES satellite observations of EMIC-wave driven relativistic electron precipitation during 1998-2010. *Journal of Geophysical Research (Space Physics)*, 118(1), 232–243. https://doi.org/10.1029/2012JA017998

Clilverd, M. A., Rodger, C. J., Gamble, R. J., Ulich, T., Raita, T., Seppälä, A., Green, J. C., N.Thomson, N. R., Sauvaud, J.-A., & Parrot, M., (2010). Ground-based estimates of outer radiation belt energetic electron precipitation fluxes into the atmosphere. *J. Geophys. Res*.,115, A12304, doi:10.1029/2010JA015638

Clilverd, M. A., Duthie, R., Hardman, R., Hendry, A. T., Rodger, C. J., Raita, T., et al. (2015). Electron precipitation from EMIC waves: A case study from 31 May 2013: Electron precipitation from EMIC-IPDP. *Journal of Geophysical Research: Space Physics*, 120(5), 3618–3631. https://doi.org/10.1002/2015JA021090

Cussac, T., Clair, M.-A., Pascale, U.-G., Buisson, F., Gerard, L.-B., Ledu, M., et al. (2006). The Demeter microsatellite and ground segment. *Planetary and Space Science*, **54**(5), 413–427. https://doi.org/10.1016/j.pss.2005.10.013

Denton, R. E., Ofman, L., Shprits, Y. Y., Bortnik, J., Millan, R. M., Rodger, C. J., da Silva, C. L., Rogers, B. N., Hudson, M. K., Liu, K., Min, K., Glocer, A., & Komar, C., (2019). Pitch angle scattering of sub-MeV relativistic electrons by electromagnetic ion cyclotron waves. *J. Geophys. Res*., 124, 5610-5626, doi:10.1029/2018JA026384

Duderstadt, K. A., Huang, C.-L., Spence, H. E., Smith, S., Blake, J. B., Crew, A. B., et al. (2021). Estimating the impacts of radiation belt electrons on atmospheric chemistry using FIREBIRD II and Van Allen Probes observations. Journal of Geophysical Research: Atmospheres, 126, e2020JD033098. https://doi.org/10.1029/2020JD033098

Engebretson, M. J., et al. (2008), Pc1–Pc2 waves and energetic particle precipitation during and after magnetic storms: Superposed epoch analysis and case studies, J. Geophys. Res., 113, A01211, doi:10.1029/2007JA012362

Evans, D. S., and M. S. Greer (2004), Polar Orbiting Environmental Satellite Space Environment Monitor–2 Instrument Descriptions and Archive Data Documentation, *NOAA Tech. Mem. 1.4*, Space Environ. Lab., Boulder, Colorado.

Fraser, B. J., & Wawrzyniak, S., (1978). Source movements associated with IPDP pulsations, *Journal of Atmospheric and Terrestrial Physics*, 40, 12, 1281-1288, https://doi.org/10.1016/0021-9169(78)90079-X

Fukunishi, H., Toya, T., Koike, K., Kuwashima, M., & Kawamura, M., (1981). Classification of hydromagnetic emissions based on frequency-time spectra. *J. Geophys. Res.*, 86, 9029-9039, . https://doi.org/10.1029/JA086iA11p09029

Fukunishi, H., (1969). Occurrence of sweepers in the evening sector following the onset of magnetospheric substorms. *Report of Ionosphere and Space Research in Japan*, 23, 21–34. Retrieved from https://ci.nii.ac.jp/naid/10006217508/en/

Gendrin, R., Lacourly, S., Troitskaya, V. A., Gokhberg, M., & Shepetnov, R. V., (1967). Caractéristiques des pulsations irrégulières de période décroissante (I. P. D. P.) et leurs relations avec les variations du flux des particules piégées dans la magnétosphère. *Planetary and Space Science*, 15(8), 1239–1240. https://doi.org/10.1016/0032-0633(67)90180-8

Gjerloev, J. W., (2012). The SuperMAG data processing technique, *J. Geophys. Res.*, 117, A09213, doi:10.1029/2012JA017683

Grison, B., Santolík, O., Lukačevič, J., & Usanova, M. E. (2021). Occurrence of EMIC waves in the magnetosphere according to their distance to the magnetopause. Geophysical Research Letters, 48, e2020GL090921. https://doi.org/10.1029/2020GL090921

Guttu, S., Orsolini, Y., Stordal, F., Otterå, O.H., Omrani,N.-E., Tartaglione, N., Verronen, P.T., Rodger, C.J. & Clilverd, M.A. (2021). Impacts of UV Irradiance and Medium-Energy Electron Precipitation on the North Atlantic Oscillation during the 11-Year Solar Cycle. Atmosphere, 12, https://doi.org/10.3390/atmos12081029

anzelka, M., Li W., & Ma Q. (2023). Parametric analysis of pitch angle scattering and losses of relativistic electrons by oblique EMIC waves. Frontiers in Astronomy and Space Sciences, 10, https://www.frontiersin.org/articles/10.3389/fspas.2023.1163515

Hanzelka, M., Li, W., Qin, M., Capannolo, L., Shen, X., Ma, Q., et al. (2024). Sub-MeV electron precipitation driven by EMIC waves through nonlinear fractional resonances. Geophysical Research Letters, 51, e2023GL107355. https://doi.org/10.1029/2023GL107355

Hendry, A. T., Rodger, C. J., Clilverd, M. A., Engebretson, M. J., Mann, I. R., Lessard, M. R., Raita, T., & Milling, D. K., (2016). Confirmation of EMIC wave-driven relativistic electron precipitation. *J. Geophys. Res. Space Physics*,121, 5366–5383, doi:10.1002/2015JA022224

Hendry, A. T., Rodger, C. J., & Clilverd, M. A., (2017). Evidence of sub-MeV EMIC-driven electron precipitation, *Geophys. Res. Lett.*, 44, 1210-1218, doi:10.1002/2016GL071807

Hendry, A. T., Santolik, O., Miyoshi, Y., Matsuoka, A., Rodger, C. J., Clilverd, M. A., et al. (2020). A multi-instrument approach to determining the source-region extent of EEP-driving EMIC waves. *Geophysical Research Letters*,47,e2019GL086599, https://doi.org/10.1029/2019GL086599

Hendry, A. T., Rodger, C. J., Clilverd, M. A., & Morley, S., (2021a). Evidence of sub-MeV EMIC-driven trapped electron flux dropouts from GPS observations, *Geophys. Res. Lett.,* 48, e2021GL092664, doi:10.1029/2021GL092664.

Hendry, A. T., Seppälä, A. Rodger, C. J., & Clilverd, M. A., (2021b). Impact of EMIC-wave driven electron precipitation on the radiation belts and atmosphere, *J. Geophys. Res.*, 126, e2020JA028671, doi:10.1029/2020JA028671

Hirai, A., Tsuchiya, F., Obara, T., Katoh, Y., Miyoshi, Y., Shiokawa, K., et al. (2023), Spatio-temporal characteristics of IPDP-type EMIC waves on April 19, 2017: Implications for loss of relativistic electrons in the outer belt. *Journal of Geophysical Research: Space Physics*, 128, e2023JA031479. https://doi.org/10.1029/2023JA031479

Jun, C.-W., Miyoshi, Y., Kurita, S., Yue, C., Bortnik, J., Lyons, L., et al. (2021). The characteristics of EMIC waves in the magnetosphere based on the Van Allen Probes and Arase observations. Journal of Geophysical Research: Space Physics, 126, e2020JA029001. https://doi.org/10.1029/2020JA029001

Katoh, Y., Rosendahl, P.S., Ogawa, Y. et al. Effect of the mirror force on the collision rate due to energetic electron precipitation: Monte Carlo simulations. Earth Planets Space 75, 117 (2023). https://doi.org/10.1186/s40623-023-01871-y

Kim, H., Lessard, M. R., Engebretson, M. J., and Lühr, H., (2010). Ducting characteristics of Pc 1 waves at high latitudes on the ground and in space. *J. Geophys. Res.*, 115, A09310, doi:10.1029/2010JA015323

Kubota, Y., and Omura, Y. (2017). Rapid precipitation of radiation belt electrons induced by EMIC rising tone emissions localized in longitude inside and outside the plasmapause. J. Geophys. Res. Space Physics, 122, 293–309, doi:10.1002/2016JA023267

Lei, F., Truscott, R. R., Dyer, C. S., Quaghebeur, B., Heynderickx, D., Nieminen, R., & Daly, E., (2002). MULASSIS: A Geant4-based multilayered shielding simulation to. *IEEE Transactions on Nuclear Science*, 49(6), 2788–2793. https://doi.org/10.1109/TNS.2002.805351

Lozinski, A. R., Horne, R. B., Glauert, S. A., Del Zanna, G., Heynderickx, D., & Evans, H. D., (2019). Solar cell degradation due to proton belt enhancements during electric orbit raising to geo. *Space Weather*, 17(7), 1059–1072. https://doi.org/10.1029/2019SW002213

Matthes, K., Funke, B., Andersson, M. E., Barnard, L., Beer, J., Charbonneau, P., et al. (2017). Solar forcing for CMIP6 (v3.2), *Geosci. Model Dev.*, 10, 2247–2302, https://doi.org/10.5194/gmd-10-2247-2017

Meredith, N. P., Horne, R. B., Kersten, T., Fraser, B. J., & Grew, R. S., (2014). Global morphology and spectral properties of EMIC waves derived from CRRES observations. *Journal of Geophysical Research: Space Physics*, 119(7), 5328–5342. https://doi.org/10.1002/2014JA020064

Millan, R., & Thorne, R., (2007). Review of radiation belt relativistic electron losses. *Journal of Atmospheric and Solar-Terrestrial Physics*, 69(3), 362–377. https://doi.org/10.1016/j.jastp.2006.06.019

Min, K., J. Lee, K. Keika, & W. Li (2012), Global distribution of EMIC waves derived from THEMIS observations, J. Geophys. Res., 117, A05219, doi:10.1029/2012JA017515.

Mironova, I.A., Aplin, K.L., Arnold, F. et al. Energetic Particle Influence on the Earth's Atmosphere. Space Sci Rev 194, 1–96 (2015). https://doi.org/10.1007/s11214-015-0185-4

Miyoshi, Y., Sakaguchi, K., Shiokawa, K., Evans, D., Albert, J., Connors, M., et al., (2008). Precipitation of radiation belt electrons by EMIC waves, observed from ground and space. *Geophysical Research Letters*, 35(23), L23101. https://doi.org/10.1029/2008GL035727

Nesse Tyssøy, H., Sinnhuber, M., Asikainen, T., Bender, S., Clilverd, M. A., Funke, B., et al. (2021). HEPPA III intercomparison experiment on electron precipitation impacts: 1. Estimated ionization rates during a geomagnetic active period in April 2010. *Journal of Geophysical Research: Space Physics*, 126, e2021JA029128. https://doi.org/10.1029/2021JA029128

Ni, B., Zhang, Y., & Gu, X, (2023). Identification of ring current proton precipitation driven by scattering of electromagnetic ion cyclotron waves, *Fundamental Research*, 3(2), 257-264, https://doi.org/10.1016/j.fmre.2021.12.018

Ohtani, S., & Gjerloev, J.W., (2020). Is the substorm current wedge an ensemble of wedgelets?: Revisit to midlatitude positive bays. *Journal of Geophysical Research: Space Physics*, 125(9), p.e2020JA027902, doi:10.1029/2020JA027902.

Orsolini, Y. J., Smith-Johnsen, C., Marsh, D. R., Stordal, F., Rodger, C. J., Verronen, P. T., & Clilverd, M. A. (2018). Mesospheric nitric acid enhancements during energetic electron precipitation events simulated by WACCM-D. Journal of Geophysical Research: Atmospheres, 123, 6984–6998. https://doi.org/10.1029/2017JD028211

Peck, E. D., Randall, C. E., Green, J. C., Rodriguez, J. V., & Rodger, C. J., (2015). POES MEPED differential flux retrievals and electron channel contamination correction, *J. Geophys. Res. Space Physics*,120,4596–4612, doi:10.1002/2014JA020817

Rodger, C. J., Raita, T., Clilverd, M. A., Seppälä, A., Dietrich, S., Thomson, N. R., & Ulich, T., (2008). Observations of relativistic electron precipitation from the radiation belts driven by EMIC waves. *Geophys. Res. Lett*., 35, L16106, doi:10.1029/2008GL034804.

Rodger, C. J., Clilverd, M. A., Green, J. & Lam, M-M., (2010). Use of POES SEM-2 observations to examine radiation belt dynamics and energetic electron precipitation in to the atmosphere, *J. Geophys. Res.*, 115, A04202, doi:10.1029/2008JA014023

Rodger, C. J., Hendry, A. T., Clilverd, M. A., Kletzing, C. A., Brundell, J. B., & Reeves, G. D. (2015). High-resolution insitu observations of electron precipitation-causing EMIC waves, Geophys. Res. Lett.,42,9633–9641, doi:10.1002/2015GL066581

Ross, J. P. J., Glauert, S. A., Horne, R.B., Watt, C. E. J., & Meredith, N. P. (2021). On the variability of EMIC waves and the consequences for the relativistic electron radiation belt population. Journal of Geophysical Research: Space Physics, 126, e2021JA029754. https://doi.org/10.1029/2021JA029754

Saikin, A. A., J.-C. Zhang, R. C. Allen, C. W. Smith, L. M. Kistler, H. E. Spence, R. B. Torbert, C. A. Kletzing, and V. K. Jordanova (2015), The occurrence and wave properties of H+-, He+-, and O+-band EMIC waves observed by the Van Allen Probes, J. Geophys. Res. Space Physics, 120, 7477–7492, doi:10.1002/2015JA021358.

Salice, J., Nesse, H., Partamies, N., Kilpua, E., Kavanagh, A., Decotte, M., Babu, E., & Smith-Johnsen, C. (2024). The high-energy tail of energetic electron precipitation: solar wind drivers and geomagnetic responses. Frontiers in Astronomy and Space Sciences, 11, https://www.frontiersin.org/articles/10.3389/fspas.2024.1352020

Salzano, M., Lessard, M. R., Noh, S., Kim, H., Waters, C., Engebretson, M. J., et al. (2022). Modeling the effects of drift shell splitting in two case studies of simultaneous observations of substorm-driven Pi1b and IPDP-type EMIC waves. *Journal of Geophysical Research: Space Physics*, 127(10), e2022JA030600. https://doi.org/10.1029/2022JA030600

Sandanger, M. I., Søraas, F., Sørbø, M., Aarsnes, K., Oksavik, K., & Evans, D. S., (2009). Relativistic electron losses related to EMIC waves during CIR and CME storms. *Journal of Atmospheric and Solar-Terrestrial Physics*, 71(10–11), 1126–1144. https://doi.org/10.1016/j.jastp.2008.07.006

Sauvaud, J.-A., Walt, M., Delcourt, D., Benoist, C., Penou, E., Chen, Y., et al., (2013). Inner radiation belt particle acceleration and energy structuring by drift resonance with ULF waves during geomagnetic storms. *J. Geophys. Res. Space Physics*,118, 1723–1736, doi:10.1002/jgra.50125

Seppälä, A., Clilverd, M. A., Beharrell, M. J., Rodger, C. J., Verronen, P. T., Andersson, M. E., & Newnham, D. A. (2015). Substorm-induced energetic electron precipitation: Impact on atmospheric chemistry. Geophys. Res. Lett., 42, 8172–8176, doi:10.1002/2015GL065523

Shen, X.-C., Li, W., Capannolo, L., Ma, Q., Qin, M., Artemyev, A. V., et al. (2023). Modulation of energetic electron precipitation driven by three types of whistler mode waves. Geophysical Research Letters, 50, e2022GL101682. https://doi.org/10.1029/2022GL101682

Sinnhuber, M., Nieder, H. & Wieters, N. Energetic Particle Precipitation and the Chemistry of the Mesosphere/Lower Thermosphere. Surv Geophys 33, 1281–1334 (2012). https://doi.org/10.1007/s10712-012-9201-3

Summers, D., & Thorne, R. M. (2003). Relativistic electron pitch-angle scattering by electromagnetic ion cyclotron waves during geomagnetic storms. *Journal of Geophysical Research (Space Physics)*, 108(A4), 1143. https://doi.org/10.1029/2002JA009489

Thorne, R. M., & Kennel, C. F. (1971). Relativistic electron precipitation during magnetic storm main phase. *J. Geophys. Res.*, 76(19), 4446–4453. https://doi.org/10.1029/JA076i019p04446

Turunen, E., Verronen, P. T., Seppälä, A., Rodger, C. J., Clilverd, M. A., Tamminen, J., et al., (2009). Impact of different precipitation energies on NOX generation during geomagnetic storms, *J. Atmos Sol.-Terr. Phys.,* 71, pp. 1176-1189, doi:10.1016/j.jastp.2008.07.005

Usanova, M. E., et al. (2014), Effect of EMIC waves on relativistic and ultra relativistic electron populations: Ground-based and Van Allen Probes observations. *Geophys. Res. Lett.*,41, 1375–1381,doi:10.1002/2013GL059024

Usanova, M. E. (2021). Energy Exchange Between Electromagnetic Ion Cyclotron (EMIC) Waves and Thermal Plasma: From Theory to Observations. *Front. Astron. Space Sci*., 8:744344, doi: 10.3389/fspas.2021.744344

van de Kamp, M., Seppälä, A., Clilverd, M. A., Rodger, C. J., Verronen, P. T., & Whittaker, I. C. (2016). A model providing long-term data sets of energetic electron precipitation during geomagnetic storms. J. Geophys. Res. Atmos., 121, 12,520–12,540, doi:10.1002/2015JD024212
van de Kamp, M., C. J. Rodger, A. Seppälä, M. A. Clilverd, and P. T. Verronen (2018). An updated model providing long-term datasets of energetic electron precipitation, including zonal dependence, *J. Geophys. Res.*, 123, 9891-9915, doi:10.1029/2017JD028253

Wang, X. Y., S. Y. Huang, R. C. Allen, H. S. Fu, X. H. Deng, M. Zhou, J. L. Burch, and R. B. Torbert (2017), The occurrence and wave properties of EMIC waves observed by the Magnetospheric Multiscale (MMS) mission, J. Geophys. Res. Space Physics, 122, 8228–8240, doi:10.1002/2017JA024237.

Whittaker, I. C., Gamble, R. J., Rodger, C. J., Clilverd, M. A., & Sauvaud, J. -A., (2013). Determining the spectra of radiation belt electron losses: Fitting DEMETER Instrument for Detecting Particle observations for typical and storm-times, *J. Geophys. Res.*, 118, doi:10.1002/2013JA019228

Yahnin, A. G., T. A. Yahnina, T. Raita, and J. Manninen (2017), Ground pulsation magnetometer observations conjugated with relativistic electron precipitation, *J. Geophys. Res.*, 122, 9169–9182, doi:10.1002/2017JA024249

Yando, K., Millan, R. M. , Green, J. C., & Evans, D. S., (2011). A Monte Carlo simulation of the NOAA POES Medium Energy Proton and Electron Detector instrument, *J. Geophys. Res*., 116, A10231, doi:10.1029/2011JA016671

Xu, W., Marshall, R. A., Tyssøy, H. N., & Fang, X. (2020). A generalized method for calculating atmospheric ionization by energetic electron precipitation. Journal of Geophysical Research: Space Physics, 125, e2020JA028482. https://doi.org/10.1029/2020JA028482

Figure Captions:

Figure 1. A map of the North Atlantic, showing the orbits of the DEMETER (blue line) and NOAA-17 (red line) spacecraft on 11 April 2005 at approximately 21:14 UT. Blue and red circles indicate the field line footprint of the satellites at the time of EMIC-induced electron precipitation. Locations are shown for the Nurmijarvi (purple square) and Halley conjugate (yellow square) induction coil magnetometers. A dashed black line indicates the L=4 contour.

Figure 2. The variation of NOAA-17 P1 and E4 fluxes between 21:13 and 21:16 UT on 11 April 2005.

Figure 3. The energy spectrum of DEMETER IDP flux during the conjunction with the NOAA 17 satellite. Enhanced fluxes are seen over the energy range 80 keV to >1 MeV. Note this is before correction of proton contamination.

Figure 4. The time variation of EMIC wave activity observed at Nurmijarvi (L=3.9) and Halley (L=4.5) respectively. Characteristic features of an IPDP wave can be seen at both sites. The white dashed lines indicate a rising frequency feature, with a rate of ~0.6 Hz/hour. The vertical white arrows indicate the time of the electron precipitation event seen by DEMETER and POES N17.

Figure 5: The variation with energy of the NOAA-17 proton flux spectra (red line) used to calculate the contamination of the DEMETER IDP instrument from those proton fluxes, after accounting for the protection afforded by the 6 μm aluminum foil using the MULASSIS code (green dashed line). The solid blue line shows the DEMETER IDP measurement at the time of the IPDP-induced precipitation, at 21:14 UT on 11 April 2005.

Figure 6: The energy spectrum of the IPDP electron precipitation fluxes determined using the DEMETER IDP instrument (blue line), and the NOAA-17 electron detectors (black line). Uncertainty ranges of ±20% are shown by dotted and dashed lines in both cases.

Figure 7: Upper panel. Fitting the energy spectrum of the corrected DEMETER IPDP electron precipitation flux using a peaked exponential function. Lower panel. Comparison of the corrected DEMETER IDP flux >200 keV with a power-law spectrum.

Figure 1.

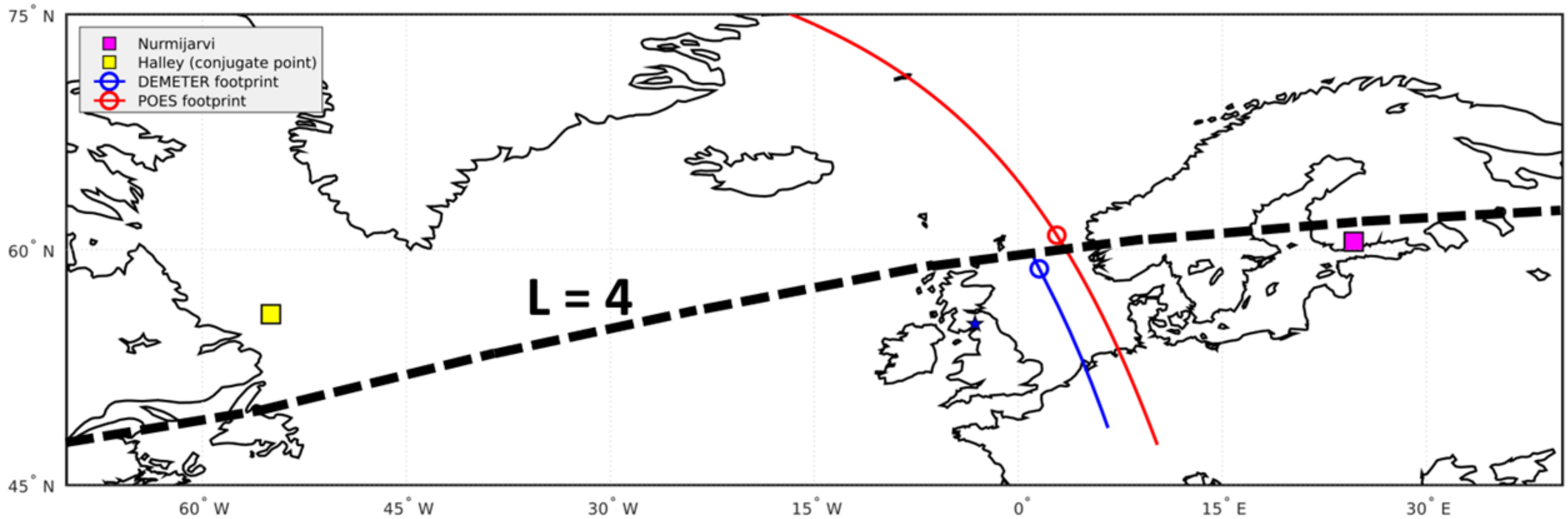

75° N
60° N
45° N
Nurmijarvi
Halley (conjugate point)
DEMETER footprint
POES footprint
L = 4
60° W
45° W
30° W
15° W
0°
15° E
30° E

Figure 2.

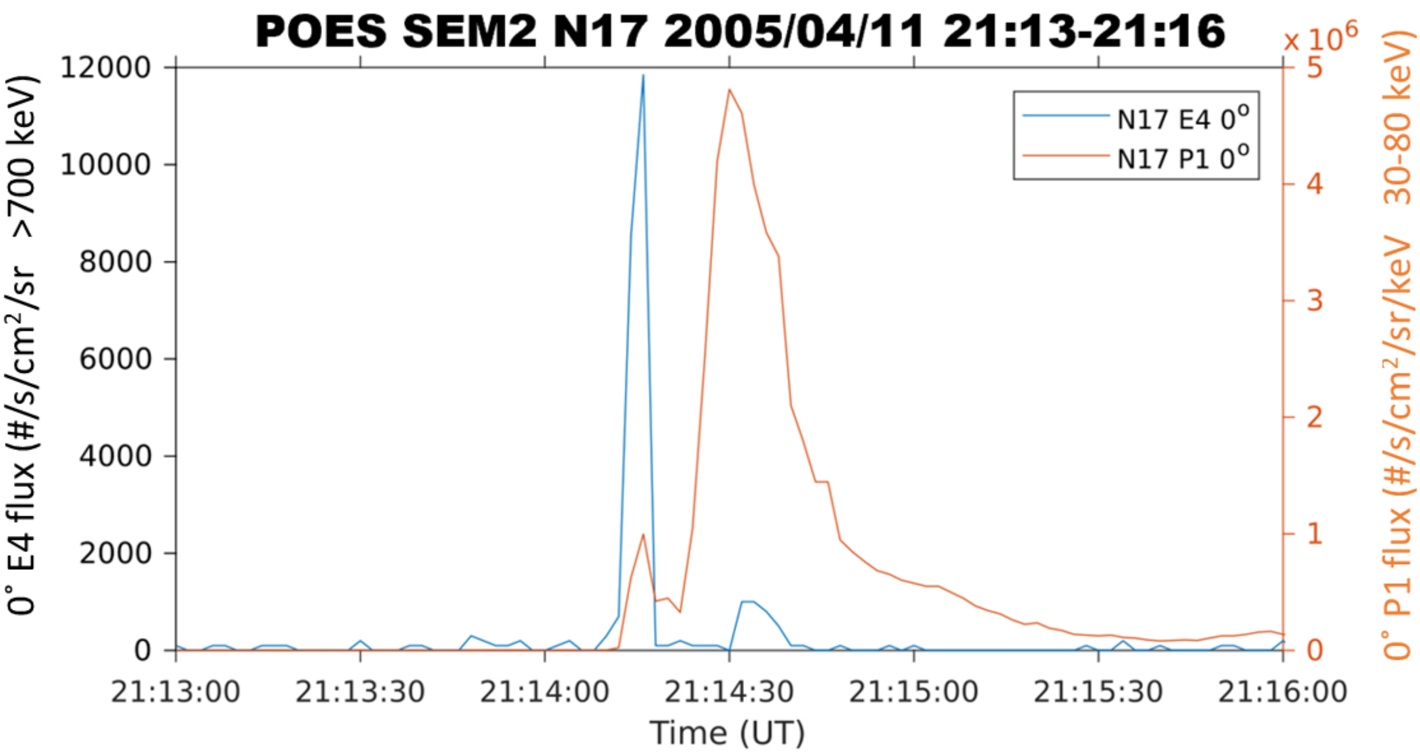
POES SEM2 N17 2005/04/11 21:13-21:16
0˚ E4 flux (#/s/cm²/sr >700 keV)
0˚ P1 flux (#/s/cm²/sr/keV 30-80 keV)
x 10⁶
N17 E4 0°
N17 P1 0°
12000
10000
8000
6000
4000
2000
0
5
4
3
2
1
0
21:13:00
21:13:30
21:14:00
21:14:30
21:15:00
21:15:30
21:16:00
Time (UT)

Figure 3.

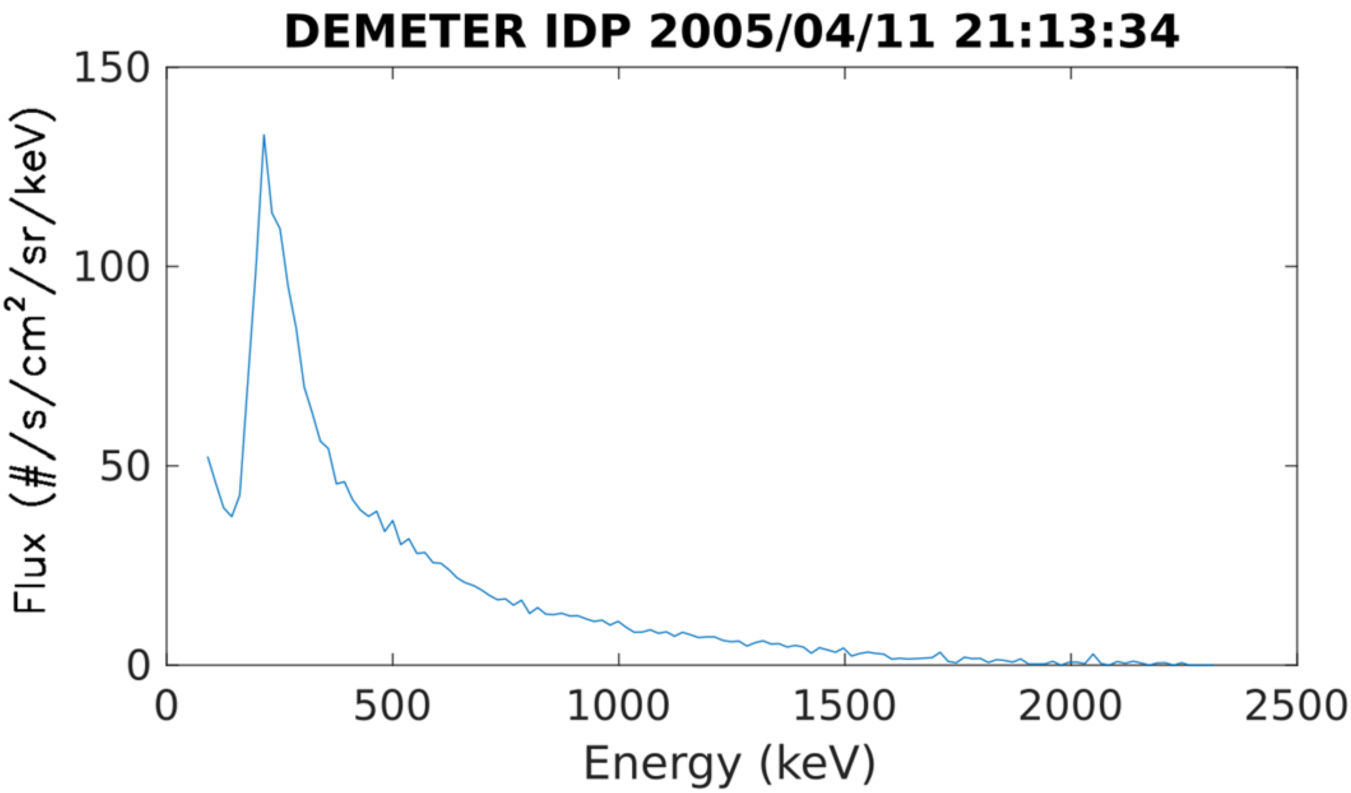
DEMETER IDP 2005/04/11 21:13:34
Flux (#/s/cm²/sr/keV)
150
100
50
0
0
500
1000
1500
2000
2500
Energy (keV)

Figure 4.

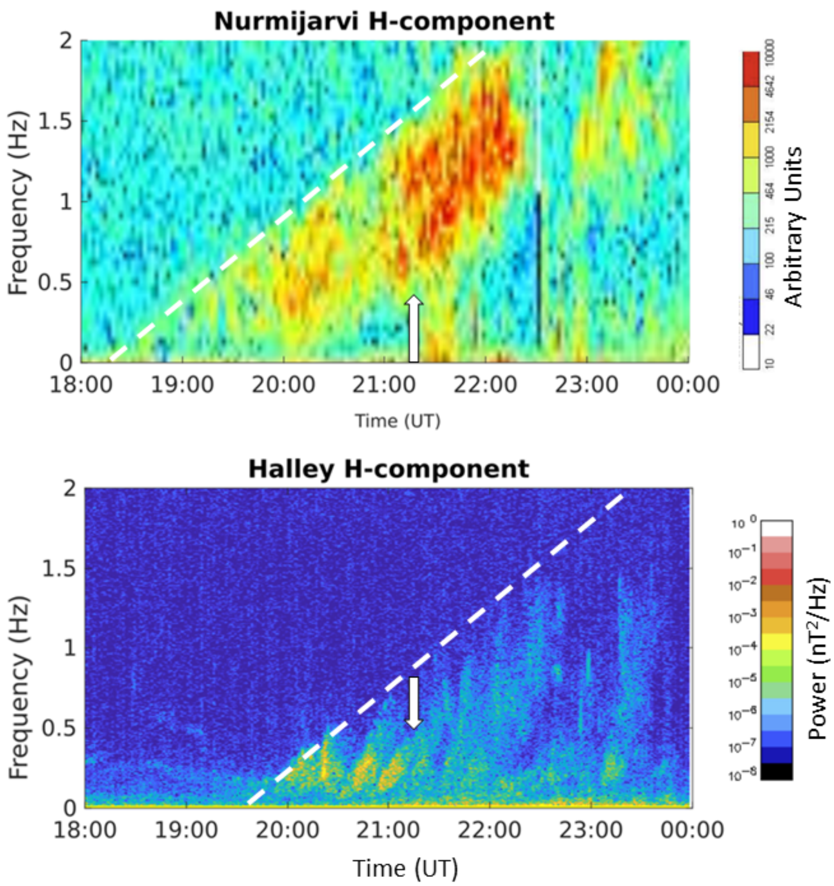
Nurmijarvi H-component
Frequency (Hz)
2
1.5
1
0.5
0
18:00
19:00
20:00
21:00
22:00
23:00
00:00
Time (UT)
10000
4642
2154
1000
464
215
100
46
22
10
Arbitrary Units
Halley H-component
Frequency (Hz)
2
1.5
1
0.5
0
18:00
19:00
20:00
21:00
22:00
23:00
00:00
Time (UT)
10^{0}
10^{-1}
10^{-2}
10^{-3}
10^{-4}
10^{-5}
10^{-6}
10^{-7}
10^{-8}
Power (nT^2/Hz)

Figure 5.

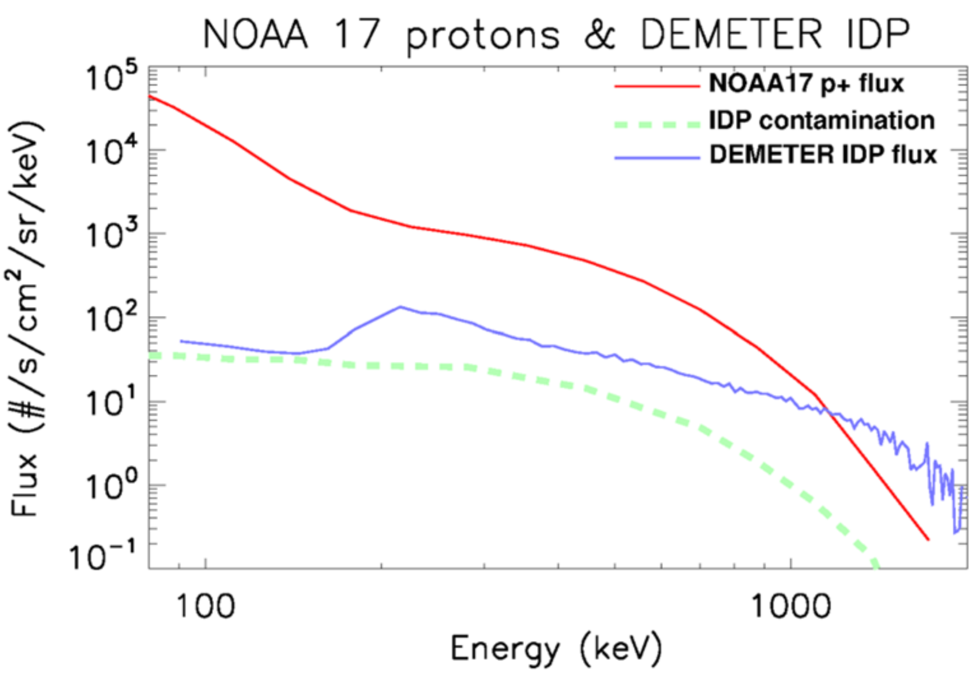

NOAA 17 protons & DEMETER IDP
NOAA17 p+ flux
IDP contamination
DEMETER IDP flux
Flux (#/s/cm²/sr/keV)
Energy (keV)

Figure 6.

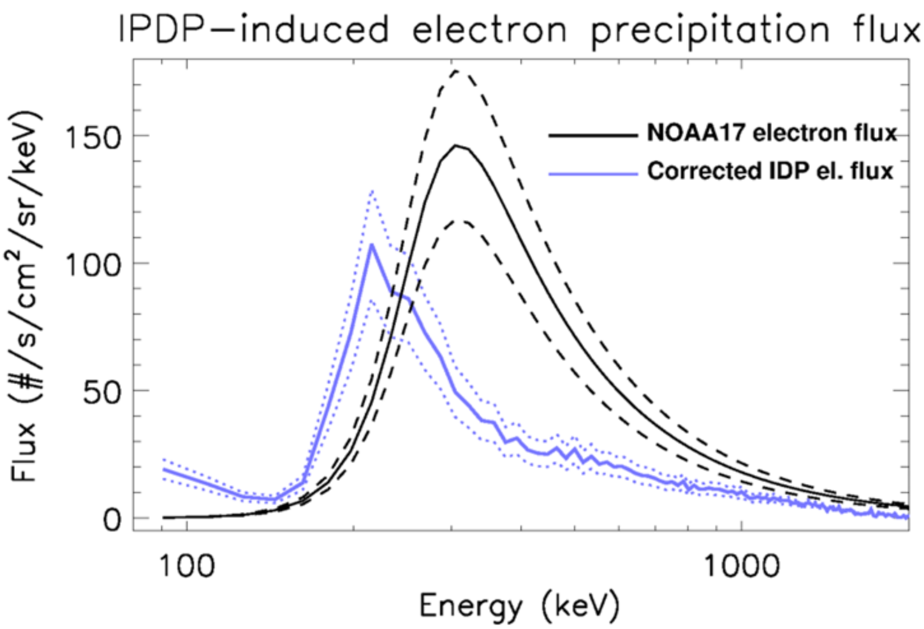

IPDP–induced electron precipitation flux
NOAA17 electron flux
Corrected IDP el. flux
Flux (#/s/cm²/sr/keV)
0
50
100
150
100
1000
Energy (keV)

Figure 7.

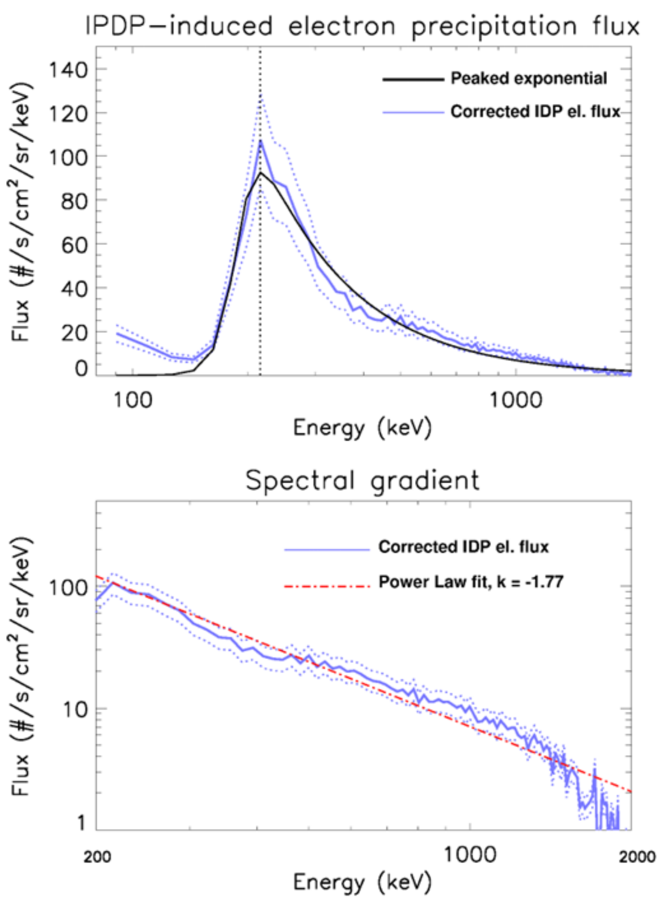

IPDP–induced electron precipitation flux
Peaked exponential
Corrected IDP el. flux
Flux (#/s/cm²/sr/keV)
140
120
100
80
60
40
20
0
100
1000
Energy (keV)
Spectral gradient
Corrected IDP el. flux
Power Law fit, k = -1.77
Flux (#/s/cm²/sr/keV)
100
10
1
200
1000
2000
Energy (keV)